

# Orientation Control of Selected Organic Semiconductor Crystals Achieved by Monolayer Graphene Templates

Lushuai Zhang, Susmit Singha Roy, Nathaniel S. Safron, Melinda J. Shearer, Robert M. Jacobberger, Vivek Saraswat, Robert J. Hamers, Michael S. Arnold, and Trisha L. Andrew\*

Crystal orientation in organic thin films is one of the key parameters that determine absorption cross-section, interfacial energetics and excitonic states, and free charge properties. In this work, monolayer graphene is used to direct the crystal orientation of selected planar organic molecules. Lying-down orientation with  $\pi$ -stacking normal to the surface is achieved with graphene templating. The absorption spectra of the graphene-templated films are correlated to molecular orientation. The same set of absorption features with or without graphene suggests that no vibronic states are forbidden or newly introduced. However, the light absorption with graphene templating is enhanced due to the altered relative orientation between the transition dipole moment of the constituent molecules and the electric field of incident light. The energy level of the highest occupied molecular orbital (HOMO) of graphene templated p-type films is observed at a deeper-lying value (relative to vacuum) compared to untemplated diindenoperylene films grown on indium tin oxide. In contrast, the HOMO energy levels of graphene templated n-type films are observed at higher-lying energy levels (relative to vacuum) compared to the respective untemplated films due to surface dipoles. Such a change can potentially increase the theoretical  $V_{oc}$  expected for photovoltaic devices incorporating these templated films.

## 1. Introduction

As most molecular organic semiconductors are anisotropic in shape, the resulting crystalline thin films have anisotropic optical and electronic characteristics that are directly affected by the molecular stacking direction. These characteristics are determined by transition dipole moment alignment and wave-function overlap between conjugated molecules.<sup>[1–4]</sup> For organic photovoltaics (OPVs), both fundamental studies and practical applications rely on artificial engineering of molecular

orientations in thin films. First of all, elucidating the effect of excited state delocalization, including singlet excitons, triplet excitons, and charge transfer states, on charge generation and recombination processes in crystalline thin films and molecular heterointerfaces requires controlled access to varied molecular orientations. A lying-down orientation provides larger out-of-plane exciton diffusion lengths and favorably increases the rate of energy transfer and charge generation and transport in molecular thin films but unfavorably increases recombination of Charge transfer (CT) states and free charges across a molecular heterointerface.<sup>[5–8]</sup> Second, the amount of total light absorbed by crystalline thin films can vary by orders of magnitude depending on the orientation of the molecular transition dipole moment relative to the electric field of incident light.<sup>[9,10]</sup> Third, the molecular orientation relative to the substrate primarily determines the energy band edge of the film.<sup>[11,12]</sup> Therefore, developing a

universal platform to gain insight into the dependence of various OPV performance parameters on molecular orientations and establishing reliable and robust methods to control the molecular orientations in thin films is necessary.

Aromatic molecules, with the notable exception of 3,4,9,10-perylenetetracarboxylic dianhydride (PTCDA) mostly adopt a standing-up orientation on weakly interacting substrates, such as oxides, which are widely used in OPVs. A lying-down molecular orientation in thin films can be achieved with thickness greater than tens of nanometers (beyond the typical thickness for OPV active layers) by quasi-epitaxial growth, in which a templating layer induces substrate–molecule interactions that are comparable to intermolecular interactions.<sup>[13]</sup> Several templating materials have been used, such as copper iodide (CuI),<sup>[14]</sup> MoS<sub>2</sub>,<sup>[15]</sup> alkali metal halide,<sup>[16]</sup> PTCDA,<sup>[17–19]</sup> and graphene.<sup>[4,13,20]</sup>

Graphene is a promising template for OPVs due to its high transparency and electrical conductivity, and its ability to be transferred onto arbitrary substrates as compared to other templating materials.<sup>[21]</sup> However, thus far, only thin films of phthalocyanine and acene molecules have been templated with graphene.<sup>[4,21]</sup> A broader study of molecular-level orientation control in various technologically relevant organic

Dr. L. Zhang, Dr. S. Singha Roy, Dr. N. S. Safron,  
Dr. R. M. Jacobberger, V. Saraswat,  
Prof. M. S. Arnold, Prof. T. L. Andrew  
Department of Materials Science and Engineering  
University of Wisconsin-Madison  
Madison, WI 53706, USA  
E-mail: tlandrew@wisc.edu

M. J. Shearer, Prof. R. J. Hamers, Prof. T. L. Andrew  
Department of Chemistry  
University of Wisconsin-Madison  
Madison, WI 53706, USA

DOI: 10.1002/admi.201600621



semiconductors using a graphene template is fundamental to building next-generation graphene-based devices.

Here, we report that graphene template layers can adjust the orientation of diverse organic molecules in thin films when using indium tin oxide (ITO) coated glass as a substrate, despite the high surface roughness of ITO. The molecules studied herein include a p-type material, diindenoperylene (DIP), and three n-type materials, 3,4,9,10-perylenetetracarboxylic bisbenzimidazole (PTCBI), pyrrolo[3,4-c]pyrrole-1,4-dione (DPP), and 1,4,5,8-naphthalenetetracarboxylic dianhydride (NTCDA). The n-type materials were chosen to enrich the set of known graphene-templated crystals, since most of the previously studied phthalocyanine and acene molecules that have been templated by graphene are p-type molecular semiconductors.

## 2. Results and Discussion

### 2.1. DIP

DIP normally adopts a standing-up orientation in thin films grown on oxides, also known as the  $\sigma$ -orientation, in which the long axis of DIP is almost normal to the surface with a mean tilt angle of  $26^\circ$  on weakly interacting substrates.<sup>[22]</sup> The topography of a DIP film on ITO (Figure 1a) is relatively smooth with a root-mean-square (RMS) roughness of 4.6 nm over 0.5  $\mu\text{m}$  image. Uniform and terrace-like domains of diameter 100–200 nm have been attributed to the  $\sigma$ -orientation of DIP.<sup>[23]</sup> Figure S1 in the Supporting Information shows the topography of bare ITO and graphene covered ITO surfaces. The RMS roughness of bare ITO is 1.2 nm, and of graphene/ITO is 0.8 nm. Figure S2a (Supporting Information) shows more structural details of the DIP crystal domains. The step heights of a domain profile shown in Figure S2c (black curve)

(Supporting Information) are comparable to the long axis of DIP, which is 1.84 nm.<sup>[22]</sup> On graphene, however, DIP domains exhibit anisotropic growth behavior. As shown in Figure S2b (Supporting Information), crystal domains form in rectangular shapes with smooth surfaces. Accordingly, the domain profile in Figure S2c (red curve) (Supporting Information) displays a plateau across the whole domain. The DIP crystal domains shown here are similar to pentacene crystal domains on oxides and graphene, which have been attributed to the standing-up and lying-down orientations, respectively.<sup>[20]</sup>

X-ray diffraction (XRD) spectra of these films (Figure 2a) confirm the lying-down crystal orientation of DIP on graphene-templated films. On ITO, the dominant  $\sigma$ -orientation is indicated by peaks at  $2\theta = 4.79^\circ$  and  $5.50^\circ$ , corresponding to  $d$ -spacing  $d = 18.46$  and  $16.06$  Å, respectively.<sup>[22,23]</sup> A weak peak at  $2\theta = 25.43^\circ$  ( $d = 3.48$  Å) is attributed to the  $\lambda$ -orientation.<sup>[22,23]</sup> DIP films grown on  $\text{SiO}_2$  substrates also display a predominant  $\sigma$ -orientation crystal phase accompanied with a small concentration of  $\lambda$ -orientation crystal phase.<sup>[23]</sup> On graphene, however, the  $\sigma$ -orientation disappears. The only peak at  $2\theta = 27.40^\circ$  ( $d = 3.25$  Å) corresponds to  $\pi$ - $\pi$  stacking normal to the surface ( $\lambda$ -orientation).<sup>[23]</sup>

Figure 3a shows the absorption spectra of 20 nm thick DIP films on bare ITO and on graphene-covered ITO. The integrated absorption is enhanced by a factor of three when the orientation changes from standing-up to lying-down because the transition dipole moment of DIP is oriented along the long axis of the molecule.<sup>[9]</sup> There is little overlap between the transition dipole of individual DIP molecules and the electric field ( $E_{xy}$ ) of incident light when DIP molecules are in a standing-up  $\sigma$ -orientation. While the molecules are lying down, the long axis and transition dipole moment become nearly parallel to  $E_{xy}$ , which enhances light coupling. This optical property change can be observed by eye, as shown in Figure S3 (Supporting Information).

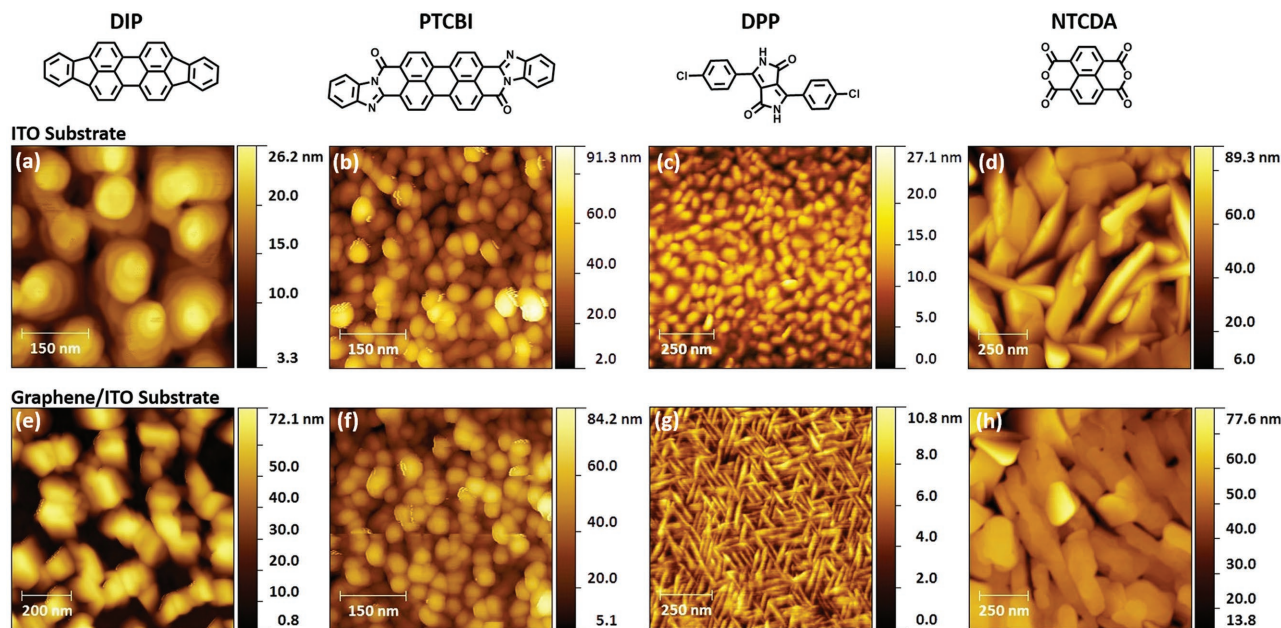
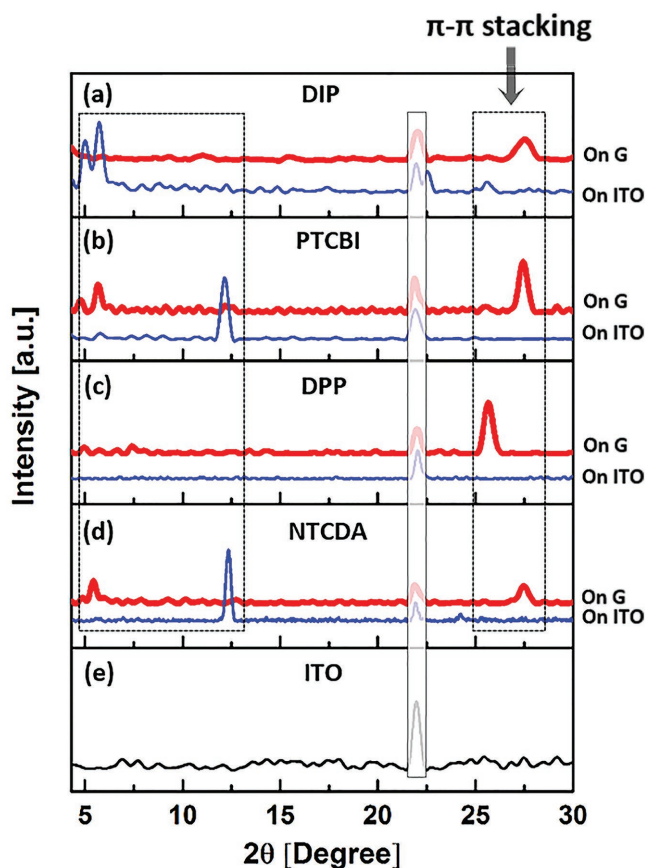


Figure 1. AFM topographic images of organic films with thickness of 50 nm grown a–d) on bare ITO and e–h) on graphene-covered ITO.



**Figure 2.** a–e) XRD spectra of organic films with thickness of 50 nm grown either on bare ITO (bottom) or on graphene-covered ITO (top). A transformation from standing-up to lying-down ( $\pi$ - $\pi$  stacking) orientation was observed in each material with graphene templating. The XRD peaks included in the box at the  $2\theta = 5^\circ$ – $15^\circ$  region correspond to standing-up orientation of molecules in the films. The peaks included in the box at the  $25^\circ$ – $30^\circ$  region correspond to  $\pi$ - $\pi$  stacking normal to the substrates in the films.

## 2.2. PTCBI

PTCBI adopts a (011) orientation on weakly interacting substrates, such as oxides, with the short axis of the molecule tilted nearly normal to the substrate.<sup>[24,25]</sup> The (001) orientation emerges on a

surface treated with self-assembled monolayers, where the long axis of the molecules are tilted normal to the substrate.<sup>[24–26]</sup> The lying-down orientation of PTCBI was previously accessed using a rubbing-assisted technique, which lead to improved power conversion efficiency in corresponding solar cells.<sup>[27]</sup>

The surface topographies of PTCBI on ITO (Figure 1b) and on graphene (Figure 1f) are identical, with both displaying uniform and dense domains. However, the XRD results in Figure 2b show dramatic differences. On ITO, only the (011) orientation with  $2\theta = 12.09^\circ$  ( $d = 7.32 \text{ \AA}$ ) exists.<sup>[24,25]</sup> On graphene, however, a majority of lying-down orientation is indicated by a dominating peak at  $2\theta = 27.40^\circ$  ( $d = 3.26 \text{ \AA}$ ), accompanied with a weak (001) peak at  $2\theta = 5.68^\circ$  ( $d = 15.6 \text{ \AA}$ ).<sup>[25,26]</sup> Figure 3b shows the absorption spectra of PTCBI films on ITO and on graphene. Both films have relatively large absorption values, which is caused by the transition dipole moment of PTCBI being oriented along the long axis of the molecule.<sup>[27,28]</sup> Hence, the transition dipole moment of PTCBI has a large coupling with incident light when the short axis is either normal to the surface (011) or  $\pi$ - $\pi$  stacking normal to surface. On graphene, the absorption of PTCBI is slightly increased and the peak corresponding to the first vibronic excitation is enhanced.

## 2.3. DPP

The DPP films have a dramatically different morphology with graphene templating, as compared to DPP films on ITO. On ITO, as shown in Figure 1c, the film exhibits small domains with RMS roughness of 3.4 nm over 1  $\mu\text{m}$  length scale. On graphene, however, DPP molecules form a dense and wire-like network with RMS roughness of 1.3 nm over 1  $\mu\text{m}$  length scale (Figure 1g). Figure S4a (Supporting Information) shows a 0.5  $\mu\text{m}$  scale atomic force microscopy (AFM) image, which clearly demonstrates ordered mesoscale aggregation. All domains align in three specific directions in plane as illustrated by the white dotted lines in Figure S4a (Supporting Information), which form a near equilateral triangle. This long-range order extends throughout the 1  $\mu\text{m}$  scale area as shown in Figure 1g. This highly ordered network most likely evolves from intermolecular hydrogen bonds between the N–H $\cdots$ O moieties in DPP. With the molecules oriented lying-down on graphene, the hydrogen bonds are confined in plane, as opposed to the DPP

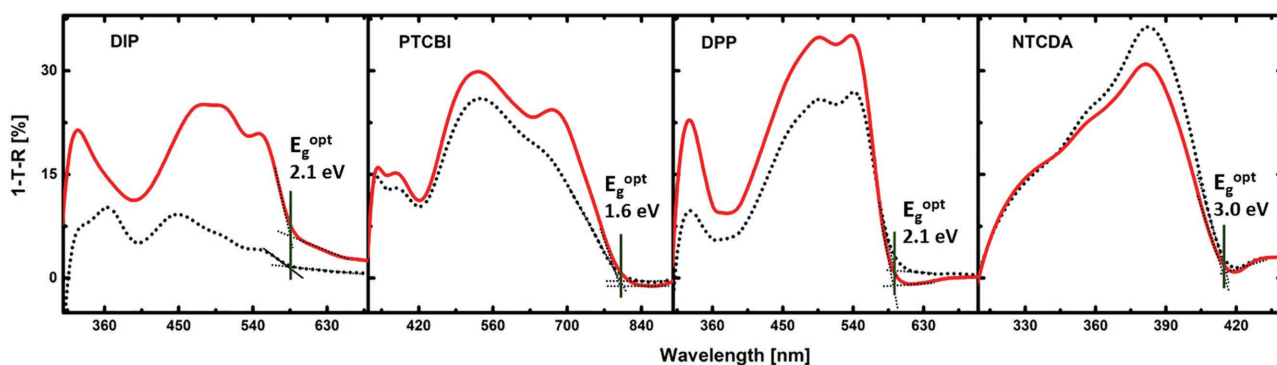


**Figure 3.** a–d) Absorption spectra of organic films with thickness of 20 nm grown either on bare ITO (dotted) or on graphene-covered ITO (solid). Measurements were taken under transmittance ( $T$ ) and reflectance ( $R$ ) modes separately. The optical bandgaps were calculated according to onset of absorption spectra.

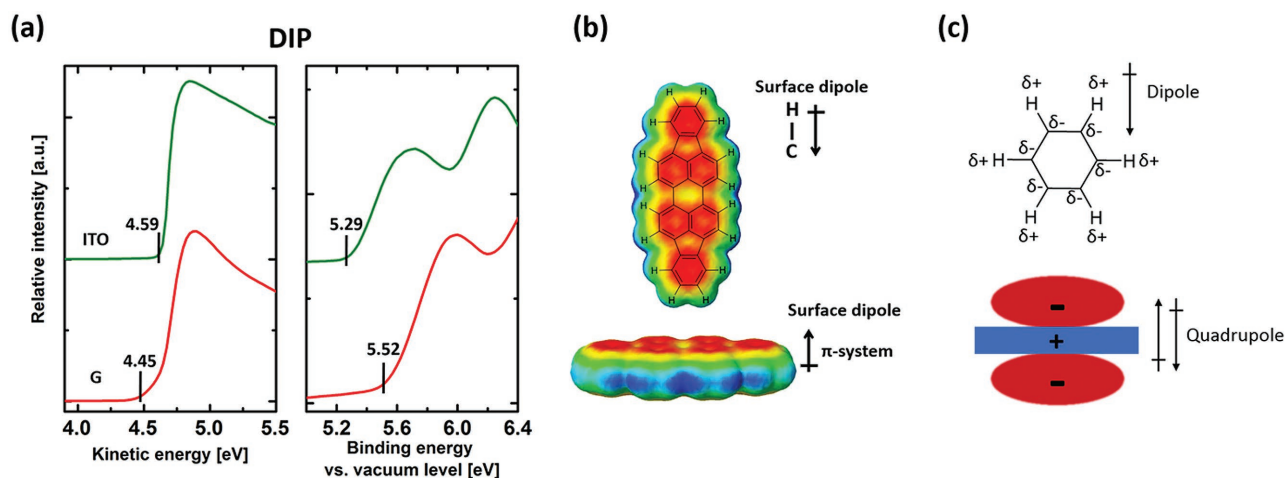


**Figure 4.** a) Secondary electron cutoff photoemission spectrum (left) and the corresponding valence band spectrum (right) of DIP on ITO (green) or on graphene/ITO (red). b) The calculated electrostatic potential surface (B3LYP 6-31G(d)) for DIP. The red regions contain the most negative electrostatic charge, blue regions contain the most positive electrostatic charge, and yellow/green regions are areas of comparatively weak negative/positive electrostatic charge. c) Illustration of six bond dipoles giving rise to a molecular quadrupole in a benzene molecule. The top image is a top-down view of benzene and the bottom image is an edge-on view.

molecules in a film grown on ITO without any dimensional confinement. Ordered 2D patterns driven by hydrogen bonding have been investigated in films of 3,3'-bis(terpyridine) and perylene tetracarboxylic diimide and its derivatives grown on graphene/Ru(0001) or on highly ordered pyrolytic graphite.<sup>[29,30]</sup> Halogen bonding may also contribute to the observed 2D order in the DPP films grown on monolayer graphene reported herein; halogen bond-initiated 2D patterns have been demonstrated in halogen-containing molecules grown on metal or on silicon.<sup>[31–33]</sup> A 3 μm length scale topographic image is displayed in Figure S4b (Supporting Information), which shows that the wire-like domains are uniformly distributed over large areas. However, long-range order on a length-scale larger than 1 μm does not exist as shown in Figure S4b (Supporting Information).

The XRD results in Figure 2c prove that DPP films are crystalline on monolayer graphene, with a substrate-normal  $\pi$ - $\pi$  stacking peak at  $2\theta = 25.58^\circ$  ( $d = 3.48 \text{ \AA}$ ), which is absent in DPP films grown in ITO. Crystalline DPP films on graphene also display significantly enhanced light absorption compared to DPP films on ITO (Figure 3c), with a peak absorbance (1-T-R) value of 35% on graphene versus 27% on ITO at 537 nm.

## 2.4. NTCDA

NTCDA on ITO readily forms a crystalline (100) phase that corresponds to the short molecular axis oriented normal to the substrate, with a herringbone structure formed in the plane of the surface.<sup>[34]</sup> The surface topographic AFM image in Figure 1d shows that the crystal domains of NTCDA on ITO differ in shapes and sizes. The domains are randomly oriented and loosely packed, with a RMS roughness of 25.1 nm over a 1 μm length scale. On graphene, NTCDA forms comparatively flatter, uniform, and densely packed crystal domains (Figure 1h), with RMS roughness of 7.7 nm over a 1 μm length scale. The surface topographic image in Figure S5 (Supporting Information) shows that the densely packed NTCDA crystal domains on graphene extend over a 5 μm length scale.

Accordingly, the XRD results in Figure 2d reveal a transformation of the (100) orientation, with  $2\theta = 12.35^\circ$  ( $d = 7.17 \text{ \AA}$ ),<sup>[34]</sup> on ITO to an ordered,  $\pi$ - $\pi$  stacked orientation normal to the surface, with  $2\theta = 27.35^\circ$  ( $d = 3.26 \text{ \AA}$ ), on graphene. The transition dipole moment of NTCDA lies along the long axis of the molecule.<sup>[35]</sup> Thus, on ITO, the transition dipole is completely parallel to  $E_{xy}$  of incident light with maximized absorption. However, when the molecules are lying down on graphene, the transition dipole is still largely in plane with  $E_{xy}$ , and so the absorption spectrum of NTCDA films on graphene does not display a significant change. A slight decrease in absorption is observed, suggesting that a small tilt angle exists between the long axis of NTCDA and the surface.

## 2.5. Ionization Potentials and Highest Occupied Molecular Orbital Energy Levels

The valence band spectra and the corresponding secondary electron cutoff photoemission spectra of 100 nm thick films of the aforementioned molecules deposited on bare ITO or on graphene/ITO were measured using ultraviolet photoelectron spectroscopy (UPS). The valence band spectra reveal the energy level values of the highest occupied molecular orbitals (HOMOs) in the condensed phase of the molecules studied herein. The valence band spectrum for DIP is shown in Figure 4a (right graph). The measured HOMO energy level values are listed in Table 1. The HOMO energy levels are 5.29 and 5.52 eV for standing-up DIP on ITO and lying-down DIP

**Table 1.** HOMO levels of organic films obtained from the valence band spectra measured by UPS.

	DIP	PTCBI	DPP	NTCDA
On ITO	5.29	6.12	6.10	7.90
On G/ITO	5.52	5.92	5.56	7.70

on graphene, respectively. The shift to a deeper energy level (relative to vacuum) upon graphene templating is attributed to surface dipoles. In analogy to well-studied seshithiophene films,<sup>[1]</sup> the dipoles associated with the arene  $C^{\delta-}-H^{\delta+}$  bonds that comprise the topmost surface of a standing-up DIP film dominate the surface potential (Figure 4b,c). The topmost surface of a lying-down DIP film, however, is dominated by the diffuse, polarizable  $\pi$ -electron cloud of DIP, which leads to the presence of an overall higher electrostatic potential over the surface of a lying-down DIP film (Figure 4b,c). Comparatively, more work is required to promote an electron from any energy level into the vacuum for lying-down DIP films due to the overall higher surface potential, leading to a larger ionization potential or, in other words, a deeper-lying HOMO level.

The calculated electrostatic potential surface of a constituent molecule can provide an intuitive method to qualitatively predict or analyze surface dipole effects on the condensed phase orbital energy levels of a molecular film.<sup>[1]</sup> Figure 4b illustrates the calculated electrostatic potential surface of DIP, calculated at the density functional theory level (B3LYP, 6-31G(d)). In this image, red regions contain the most negative electrostatic charge, blue regions contain the most positive electrostatic charge, and yellow/green regions are areas of comparatively weak negative/positive electrostatic charge. As is expected for a polycyclic aromatic hydrocarbon, DIP has a quadrupole moment that arises because an  $sp^2$  C is more electronegative than H. The vector sum of all the sixteen  $C^{\delta-}-H^{\delta+}$  bond dipoles

in DIP yields a significant molecular quadrupole moment (positive electrostatic charge in the plane of the molecule and negative electrostatic charge above and below the plane of the molecule), similar to benzene (Figure 4c). For a standing-up DIP film, the  $C^{\delta-}-H^{\delta+}$  bond dipoles on the surface point toward the film below. Upon lying down, the surface dipole points away from the positively charged molecular plane, toward the negatively charged  $\pi$ -electron cloud lying above the plane of the molecule. This change in surface dipole orientation leads to a higher ionization potential and, thus, deeper-lying HOMO levels for graphene templated p-type DIP films.

In contrast, graphene templated films of all the n-type molecules studied in this work show higher-lying HOMO levels (with lowered ionization potentials) compared to the respective films grown on ITO. The effect of electron-withdrawing heteroatoms on the ionization potentials of perfluorinated copper(II) phthalocyanine molecules in the standing-up orientation has been previously studied;<sup>[36]</sup> however, analogous reports on n-type molecules in the lying-down orientation are rare.<sup>[37]</sup> The valence band spectra for PTCBI, DPP, and NTCDA, the calculated electrostatic potential surfaces (B3LYP, 6-31G(d)) for each molecule, as well as the illustration of bond dipoles and molecular quadrupole of hexafluorobenzene as a model molecule, are shown in Figure 5. The HOMO energy level values are summarized in Table 1. These molecules have a common electron-withdrawing carbonyl functional group, and PTCBI has an additional electron-withdrawing imine moiety. PTCBI and NTCDA both adopt

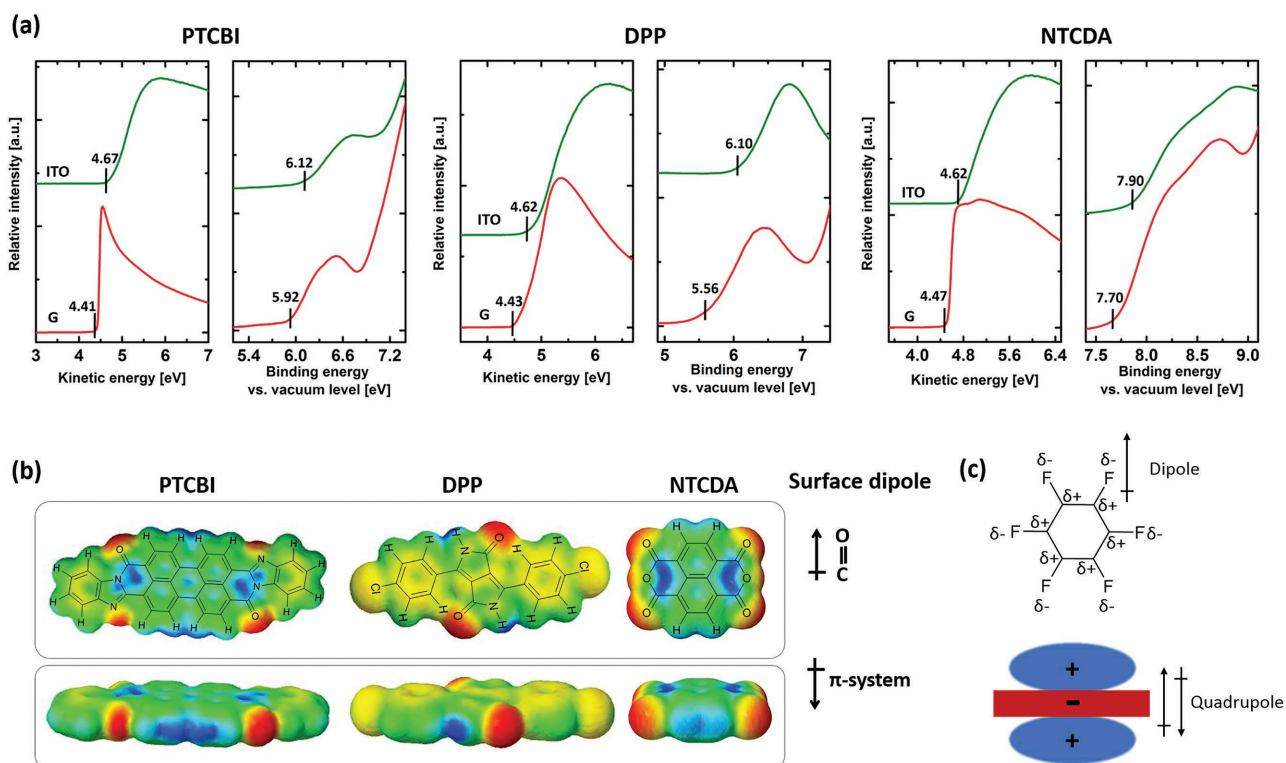


**Figure 5.** a) Secondary electron cutoff photoemission spectra (left) and the corresponding valence band spectra (right) of PTCBI, DPP, and NTCDA on ITO (green) or on graphene/ITO (red). b) Calculated electrostatic potential surfaces (B3LYP, 6-31G(d)) for PTCBI, DPP, and NTCDA. The red regions contain the most negative electrostatic charge, blue regions contain the most positive electrostatic charge, and yellow/green regions are areas of comparatively weak negative/positive electrostatic charge. c) Illustration of six bond dipoles giving rise to a molecular quadrupole in a hexafluorobenzene molecule. The top image is a top-down view of hexafluorobenzene and the bottom image is an edge-on view.

an orientation on ITO where the short axis of the molecule is normal to the surface. The carbonyl moiety in both molecules, as well as the imine moiety in PTCBI, dominate the surface dipole in a standing-up orientation, where the dipole moment points away from surface, as shown in Figure 5b. DPP forms a film on ITO in which some carbonyl groups are exposed to the surface. Although these exposed carbonyl groups are randomly oriented, the dipoles point toward the edge of molecules from the core—in other words, away from the surface of a film—as they would in a crystalline film with standing-up molecules. Such strong surface dipoles pointing away from the surface lead to increased ionization potentials and, thus, deeper-lying HOMO energy levels in films of standing-up n-type molecules grown on ITO.

Similar to the lying-down DIP films discussed above, the top-most surfaces of lying-down films of PTCBI, NTCDA, and DPP are dominated by the diffuse, polarizable  $\pi$ -electron cloud of the respective molecules. However, the quadrupole moments of PTCBI, NTCDA, and DPP are inverted compared to that of DIP and benzene, with negative electrostatic charge found in the plane of the molecule and positive electrostatic charge found above and below the plane of the molecule—i.e., the  $\pi$ -electron clouds of these electron deficient arenes are regions of positive electrostatic charge. This kind of inverted quadrupole moment, which is opposite in sign to that of a typical polycyclic aromatic hydrocarbon, is similar to the inverted quadrupole moment of hexafluorobenzene (Figure 5c) and is expected for any arene substituted with electron withdrawing groups that leave the  $sp^2$  C with a  $\delta^+$  charge. Therefore, the surface dipoles in lying-down films of PTCBI, NTCDA, and DPP point toward the surface, leading to decreased ionization potentials and, thus, higher-lying HOMO energy levels compared to standing-up films of the same molecules.

The ramifications of tuning the orbital energy levels of n-type molecular semiconductors by simply changing molecular orientation can be underscored by considering two different Type II heterojunctions where only the molecular orientation and, therefore, energy level, of one layer is varied. We note that, for real applications of each particular heterojunction, ground-state charge-transfer induced band-bending and interface dipole induced vacuum level shifts need to be taken into account for the most accurate quantitative analysis. Figure 6 provides a picture to qualitatively demonstrate the critical roles that molecular orientations can play for solar cell applications by using the energy levels measured on each single film. Take the tetraphenylidibenzoperiflanthene (DBP)/DPP donor/acceptor type II heterojunction as an example. As shown in Figure 6, the orbital energy levels measured for a standing-up DIP film are used to represent the donor component in both Type II heterojunctions. The lowest unoccupied molecular orbital (LUMO) energy levels used for both DIP and DPP were obtained by adding together the HOMO energy levels (measured by UPS) and the optical bandgaps revealed by the 1-T-R spectra shown in Figure 3. The predicted maximum open circuit voltage ( $V_{oc}$ ) of a DIP–DPP heterojunction can be increased from a theoretical value of 1.29 to 1.83 V, by simply changing the molecular orientation of DPP. A 0.54 V increase in photovoltage is dramatic, especially since multiple-step chemical syntheses and iterative, trial-and-error experiments would be necessary to achieve the

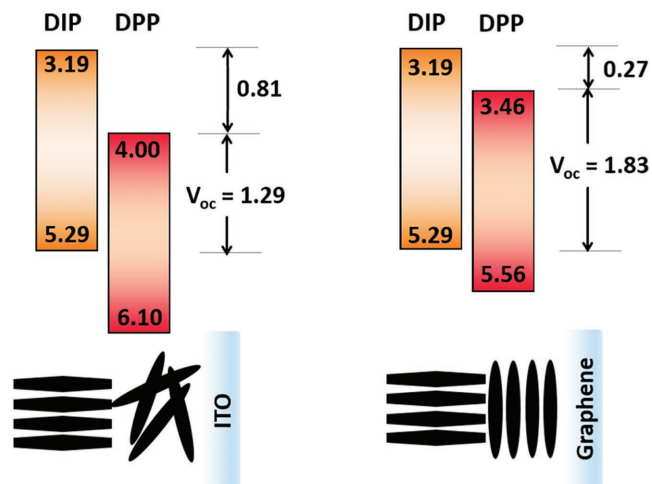


**Figure 6.** Schematic illustration of two DIP–DPP heterojunctions where the molecular orientation and, therefore, energy level of DPP is varied.

same result by changing the chemical structure of the electron acceptor component. The energy level offset between the LUMOs of the electron donor and acceptor is also decreased from 0.81 to 0.27 eV upon changing the molecular orientation of DPP. This smaller LUMO offset is favorable in that it mitigates the theoretical amount of energy lost in the heterojunction. However, a smaller LUMO offset may also lead to lower exciton dissociation efficiencies in the heterojunction.

Indeed, the two DIP–DPP heterojunctions depicted in Figure 6 are a perfect test bed to probe molecular orientation-dependent exciton dissociation/recombination events, potential hot exciton dissociation,<sup>[5,38]</sup> and molecular orientation-dependent interfacial charge transfer states in well-defined molecular heterojunctions. Using the same electron donor/acceptor materials and simply tuning energy levels by changing the molecular orientation of one of the components is a practical solution to study interfacial properties in OPVs, especially when combined with careful theoretical studies. Otherwise, energy level tuning can only be effected by developing new materials, which introduces new variables and presents other experimental difficulties.

### 3. Conclusion

The molecular orientations of one p-type material, DIP, and three n-type organic semiconductors, PTCBI, DPP, and NTCDA, were tuned by using monolayer graphene as a template. AFM, XRD, and absorption spectroscopy prove that the molecular orientations of these organic molecules were transformed from standing-up on ITO to lying-down on graphene. Additionally, DPP exhibits confined in-plane growth, giving rise to ordered molecular aggregates displaying mesoscale order over 1  $\mu\text{m}$ . Significantly enhanced light absorption was observed in DIP and DPP films templated by graphene due to increased overlap between the molecular transition dipole moment and the electric field of incident light. The dramatic change of energy levels and interfacial energetics upon graphene templating is favorable for enhancing  $V_{oc}$  when

incorporated into a device. Thus, graphene is an appealing, atomically thin material for tuning the orientation and morphology of small molecule organic semiconductor films to ultimately improve optoelectronic device performance.

#### 4. Experimental Section

Monolayers of graphene were grown on Cu foils via chemical vapor deposition. The foils were cleaned with acetic acid and deionized water, followed by annealing at 1030 °C in a flow of 350 sccm of 95% argon and 5% hydrogen. The growth was conducted at 1030 °C with an additional flow of 0.3 sccm of 95% argon and 5% methane. After growth, the graphene films were transferred onto ITO/glass substrates using poly(methyl methacrylate) (PMMA) sacrificial layers.<sup>[21,39]</sup> To remove the PMMA layer, the samples were placed in room-temperature acetone baths ( $\times 2$ ) for 20 min after which they were rinsed in isopropanol for 2 min to wash away any residual acetone. Finally, they were dried using an air gun and then annealed in an Ar atmosphere for 2 h at 500 °C to remove any residual PMMA. Organic molecules were deposited by thermal evaporation under high vacuum ( $< 2 \times 10^{-6}$  torr)<sup>[13]</sup> with a deposition rate of  $0.3 \text{ \AA s}^{-1}$ . The thicknesses of the deposited films were monitored in situ by a quartz crystal microbalance. The morphologies of the films were characterized in air using an Agilent 5500 atomic force microscope. The film crystallinity and orientation were characterized using a Bruker D8 Discover X-ray diffractometer in the  $\theta$ - $2\theta$  configuration with Cu K $\alpha$  (wavelength = 1.542 Å) source. Absorption spectra were recorded using an Evolution 220 UV-visible spectrophotometer with ISA 220 integrating sphere under reflectance and transmittance mode. Light beam is normal to the substrates. The optical bandgap  $E_{\text{opt}}$  of the films are estimated by linear extrapolation from the absorption feature edge to baseline and subsequent conversion of the wavelength (nm) into energy value versus vacuum (eV). Films used for AFM and XRD studies were 50 nm thick, and for absorption measurements were 20 nm thick. Five different spots on each film were characterized. UPS measurements were conducted in a home-built UHV multichamber system (PHI Electronics Inc., Eden Prairie, MN) with base pressure better than  $1 \times 10^{-9}$  Torr. A helium discharge lamp with energy  $h\nu = 21.22$  eV was used as the UPS source, and the photoelectrons produced were measured at a  $0^\circ$  electron take-off angle by a model 10-360 hemispherical analyzer. The bias voltage applied was  $-12$  V. The UPS spectra shown in Figures 4 and 5 were shifted to account for the applied bias.

#### Supporting Information

Supporting Information is available from the Wiley Online Library or from the author.

#### Acknowledgements

All authors have given approval to the final version of the manuscript. The authors gratefully acknowledge the support from the University of Wisconsin Materials Research Science and Engineering Center (DMR-1121288). Partial support is acknowledged by MSA and SSR for graphene synthesis and transfer, from the National Science Foundation (Grant No. CBET-1033346) and the DOE Office of Science Early Career Research Program (Grant No. DE-SC0006414) through the Office of Basic Energy Sciences.

Received: June 30, 2016

Revised: September 4, 2016

Published online:

- [1] S. Duhm, G. Heimel, I. Salzmann, H. Glowatzki, R. L. Johnson, A. Vollmer, J. P. Rabe, N. Koch, *Nat. Mater.* **2008**, *7*, 326.  
[2] G. Heimel, I. Salzmann, S. Duhm, N. Koch, *Chem. Mater.* **2010**, *23*, 359.

- [3] S. Varughese, *J. Mater. Chem. C* **2014**, *2*, 3499.  
[4] W. H. Lee, J. Park, S. H. Sim, S. Lim, K. S. Kim, B. H. Hong, K. Cho, *J. Am. Chem. Soc.* **2011**, *133*, 4447.  
[5] A. E. Jailaubekov, A. P. Willard, J. R. Tritsch, W.-L. Chan, N. Sai, R. Gearba, L. G. Kaake, K. J. Williams, K. Leung, P. J. Rossky, X. Y. Zhu, *Nat. Mater.* **2013**, *12*, 66.  
[6] Y. Yi, V. Coropceanu, J.-L. Brédas, *J. Am. Chem. Soc.* **2009**, *131*, 15777.  
[7] B. Bernardo, D. Cheyns, B. Verreert, R. D. Schaller, B. P. Rand, N. C. Giebink, *Nat. Commun.* **2014**, *5*, 3245.  
[8] S. Verlaak, D. Beljonne, D. Cheyns, C. Rolin, M. Linares, F. D. R. Castet, J. R. M. Cornil, P. Heremans, *Adv. Funct. Mater.* **2009**, *19*, 3809.  
[9] C. Schünemann, D. Wynands, K.-J. Eichhorn, M. Stamm, K. Leo, M. Riede, *J. Phys. Chem. C* **2013**, *117*, 11600.  
[10] O. Guskova, C. Schünemann, K.-J. Eichhorn, K. Walzer, M. Levichkova, S. Grundmann, J.-U. Sommer, *J. Phys. Chem. C* **2013**, *117*, 17285.  
[11] J. Q. Zhong, H. Y. Mao, R. Wang, D. C. Qi, L. Cao, Y. Z. Wang, W. Chen, *J. Phys. Chem. C* **2011**, *115*, 23922.  
[12] S. Zhong, J. Q. Zhong, H. Y. Mao, J. L. Zhang, J. D. Lin, W. Chen, *Phys. Chem. Chem. Phys.* **2012**, *14*, 14127.  
[13] L. Zhang, S. S. Roy, C. R. English, R. J. Hamers, M. S. Arnold, T. L. Andrew, *ACS Nano* **2015**, *9*, 2510.  
[14] C. H. Cheng, J. Wang, G. T. Du, S. H. Shi, Z. J. Du, Z. Q. Fan, J. M. Bian, M. S. Wang, *Appl. Phys. Lett.* **2010**, *97*, 083305.  
[15] R. S. C. Ludwig, J. Petersen, B. Gompf, W. Eisenmenger, *J. Vac. Sci. Technol. B* **1994**, *12*, 1963.  
[16] R. R. Lunt, J. B. Benziger, S. R. Forrest, *Adv. Mater.* **2007**, *19*, 4229.  
[17] R. R. Lunt, B. E. Lassiter, C. K. Renshaw, S. R. Forrest, *Opt. Express* **2010**, *18*, A444.  
[18] K. V. Chauhan, P. Sullivan, J. L. Yang, T. S. Jones, *J. Phys. Chem. C* **2010**, *114*, 3304.  
[19] S. Heutz, R. Cloots, T. S. Jones, *Appl. Phys. Lett.* **2000**, *77*, 3938.  
[20] L. Zhang, S. S. Roy, R. J. Hamers, M. S. Arnold, T. L. Andrew, *J. Phys. Chem. C* **2015**, *119*, 45.  
[21] S. Singha Roy, D. J. Bindl, M. S. Arnold, *J. Phys. Chem. Lett.* **2012**, *3*, 873.  
[22] A. C. Dürr, N. Koch, M. Kelsch, A. Rühm, J. Ghijsen, R. L. Johnson, J. J. Pireaux, J. Schwartz, F. Schreiber, H. Dosch, A. Kahn, *Phys. Rev. B* **2003**, *68*, 115428.  
[23] A. C. Dürr, B. Nickel, V. Sharma, U. Täffner, H. Dosch, *Thin Solid Films* **2006**, *503*, 127.  
[24] P. Dhagat, H. M. Haverinen, R. J. Kline, Y. Jung, D. A. Fischer, D. M. DeLongchamp, G. E. Jabbour, *Adv. Funct. Mater.* **2009**, *19*, 2365.  
[25] J. Mizuguchi, *Acta Crystallogr. Sect. E* **2005**, *61*, o1064.  
[26] W. H. Lee, J. H. Cho, K. Cho, *J. Mater. Chem.* **2010**, *20*, 2549.  
[27] T. Matsushima, H. Matsuo, T. Yamamoto, A. Nakao, H. Murata, *Sol. Energy Mater. Sol. Cells* **2014**, *123*, 81.  
[28] H. Tanaka, T. Yasuda, K. Fujita, T. Tsutsui, *Adv. Mater.* **2006**, *18*, 2230.  
[29] C. Meier, M. Roos, D. Künzel, A. Breitruck, H. E. Hoster, K. Landfester, A. Gross, R. J. Behm, U. Ziener, *J. Phys. Chem. C* **2010**, *114*, 1268.  
[30] M. Roos, B. Uhl, D. Künzel, H. E. Hoster, A. Gross, R. J. Behm, *Beilstein J. Nanotechnol.* **2011**, *2*, 365.  
[31] R. Gutzler, C. Fu, A. Dadvand, Y. Hua, J. M. MacLeod, F. Rosei, D. F. Perepichka, *Nanoscale* **2012**, *4*, 5965.  
[32] R. Gutzler, O. Ivasenko, C. Fu, J. L. Brusso, F. Rosei, D. F. Perepichka, *Chem. Commun.* **2011**, *47*, 9453.  
[33] K. R. Harikumar, T. Lim, I. R. McNab, J. C. Polanyi, L. Zotti, S. Ayissi, W. A. Hofer, *Nat. Nanotechnol.* **2008**, *3*, 222.

- [34] R. R. Lunt, K. Sun, M. Kröger, J. B. Benziger, S. R. Forrest, *Phys. Rev. B* **2011**, *83*, 064114.
- [35] M. Makowski, P. Zazakowny, M. T. Pawlikowski, *J. Raman Spectrosc.* **2013**, *44*, 1548.
- [36] W. Chen, D.-C. Qi, H. Huang, X. Gao, A. T. S. Wee, *Adv. Funct. Mater.* **2011**, *21*, 410.
- [37] I. Salzmänn, A. Moser, M. Oehzelt, T. Breuer, X. Feng, Z.-Y. Juang, D. Nabok, R. G. Della Valle, S. Duhm, G. Heimel, A. Brillante, E. Venuti, I. Bilotti, C. Christodoulou, J. Frisch, P. Puschnig, C. Draxl, G. Witte, K. Müllen, N. Koch, *ACS Nano* **2012**, *6*, 10874.
- [38] K. Vandewal, S. Albrecht, E. T. Hoke, K. R. Graham, J. Widmer, J. D. Douglas, M. Schubert, W. R. Mateker, J. T. Bloking, G. F. Burkhard, A. Sellinger, J. M. J. Fréchet, A. Amassian, M. K. Riede, M. D. McGehee, D. Neher, A. Salleo, *Nat. Mater.* **2014**, *13*, 63.
- [39] X. Li, Y. Zhu, W. Cai, M. Borysiak, B. Han, D. Chen, R. D. Piner, L. Colombo, R. S. Ruoff, *Nano Lett.* **2009**, *9*, 4359.
-